FIB-SEM and X-ray CT characterization of interconnected pores in high-rank coal formed from regional metamorphism

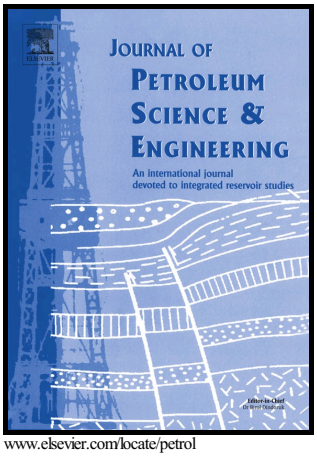

www.elsevier.com/locate/petrol

FIB-SEM and X-ray CT characterization of interconnected pores in high-rank coal formed from regional metamorphism

Shiqi Liu, Shuxun Sang, Geoff Wang, Jingsheng Ma, Xin Wang, Wenfeng Wang, Yi Du, Tian Wang

PII: S0920-4105(16)30580-0
DOI: http://dx.doi.org/10.1016/j.petrol.2016.10.006
Reference: PETROL3666

To appear in: *Journal of Petroleum Science and Engineering*

Received date: 29 March 2016
Revised date: 29 September 2016
Accepted date: 4 October 2016

Cite this article as: Shiqi Liu, Shuxun Sang, Geoff Wang, Jingsheng Ma, Xi Wang, Wenfeng Wang, Yi Du and Tian Wang, FIB-SEM and X-ray CT characterization of interconnected pores in high-rank coal formed from regiona metamorphism, *Journal of Petroleum Science and Engineering* http://dx.doi.org/10.1016/j.petrol.2016.10.006

FIB-SEM and X-ray CT characterization of interconnected pores in high-rank coal formed from regional metamorphism

Shiqi Liu[a], Shuxun Sang[b*], Geoff Wang[c], Jingsheng Ma[d], Xin Wang[e], Wenfeng Wang[b], Yi Du[b], Tian Wang[b]

[a]The Key Laboratory of Coal-based CO_2 Capture and Geological Storage, Jiangsu Province, Low Carbon Energy Institute, China University of Mining and Technology, Xuzhou 221116, China

[b]Key Laboratory of Coalbed Methane Resources and Reservoir Formation Process, Ministry of Education, School of Mineral Resource and Geoscience, China University of Mining and Technology, Xuzhou 221116, China

[c]School of Chemical Engineering, The University of Queensland, Brisbane, QLD 4072, Australia

[d]Institute of Petroleum Engineering, Heriot-Watt University, Edinburgh, EH14 4AS, United Kingdom

[e]Institute of Oceanographic Instrumentation, Shandong Academy of Sciences (SDIOI), Qingdao, 266001, China

[*]Corresponding Author. Telephone: +86-516-83590259; Fax: +86-516-83590259. E-mail: shxsang@cumt.edu.cn (S.-X. Sang)

Abstract:

Pores in coal and their connectivity are important properties of coal, providing network or channels for gas storage and migration within coal, e.g. during the coalbed methane (CBM) recovery. To investigate the growth characteristics and genetic types of pores in coal in terms of macropore and mesopore, the pores of a high-rank coal were measured by various techniques such as the mercury intrusion method, nitrogen adsorption, focused ion beam scanning electron microscopy (FIB-SEM), and X-ray micro-CT (Computed Tomography). Two high-rank coals formed from regional metamorphism collected from the southern Qinshui basin were selected. The FIB-SEM and X-ray micro-CT provides detailed experimental information for development of a three dimensional (3D) pore network model, which was further used to characterize the pore connectivity. Volume percent of pores of these high-rank coals are dominated by mesopores of approximately 10-50 nm in width, and then followed by micropores, along with the smallest volume percent of macropores. The connectivity within this high-rank coal was mesopore-dominated pore network. Electron microscopy observations further revealed there are coalification-related pores and mineral-related pores in the high-rank coal. The coalification-related pores can be classified as secondary gas pores in organic matter and shrinkage-induced pores around quartz and clay minerals; and the mineral-related pores are developed within minerals, and can be classified as dissolution-created pores and intercrystalline pores. The secondary gas pores are macropores and have poor connectivity. The mineral-related pores can be both macropores and mesopores, and have little influence on pore connectivity due to small content of carbonate minerals in these samples. Under electron microscopy, the shrinkage-induced pores are mainly mesopores. The regional metamorphism, with a high abnormal old thermal field in the research area, is the precondition of the formation of the shrinkage-induced pores. The quartz and clay minerals in the coal provide different formation conditions and hence form different shapes of the shrinkage-induced pores. The coal samples include a large number of shrinkage-induced pores that act as the interconnected pores in the coal and exhibit good connectivity. The quartz and clay minerals play a significant role in developing the interconnected pores in the high-rank coal formed from regional metamorphism.

Keywords: Pore; Mineral; Pore connectivity; Regional metamorphism; High-rank coal; Southern Qinshui basin

1. Introduction

Pores are the major reservoir sites of coalbed methane (CBM) and are considered to be important channels of CBM output (Liu et al., 2014a, 2015b, c; Sang et al., 2009; Weishauptova et al., 2004). The development degree of pores and pore connectivity in coal determine the coal porosity and permeability (Alexeev et al., 1999; Liu et al., 2014a, 2015b, c; Sang et al., 2009; Weishauptova et al., 2004). The growth characteristics of pores, such as geneses, types, structures, sizes, and fractal features can affact gas content, gas migration, contact angle of fluid, and further the CBM exploitation (Alexeev et al., 2007; Alexeev et al., 2004; Crosdale et al., 1998; Gürdal and Yalçın, 2001; Liu et al., 2015b; Moore, 2012; Weishauptova et al., 2004; Yao et al., 2010). Therefore, understanding the growth characteristics and connectivity of pores in coal is of great significance for CBM exploration and exploitation.

Coals with different ranks have different growth characteristics of pores due to the lithostatic pressure, tectonism, and degree of metamorphism (Gan et al., 1972; Hakimi et al., 2013; Wang et al., 2009; Zhou et al., 2015). During the early stages of coalification (usually corresponding to the mean maximum reflectance values of vitrinite $R_{o,max}$<0.65 %), the aromatic layer of coal is small and nearly randomly distributed (Bao et al., 2013; Hirsch, 1954; Xia et al., 2013; Zhou et al., 2015). Pores in such coals are developed in each scale of pore width with large pore volume and internal surface area (Bao et al., 2013; Xia et al., 2013; Zhou et al., 2015). During the high-volatile bituminous coal and medium-volatile bituminous coal stages ($R_{o,max}$=0.65-1.2 %), with the increase in coal rank and under the mechanical compaction and dehydration effects, pore volume reduces, especially macropores and mesopores (Bao et al., 2013; Liu et al., 2013; Xia et al., 2013; Zhou et al., 2015). At the low-volatile bituminous coal stage ($R_{o,max}$=1.3-1.7%), humic gelation completes dehydration and compaction, and the micropore content furtherdeclines. During the high-rank coal stage ($R_{o,max}$>1.9 %), the aromatic ring has a directional alignment, forming a series of micropores, mainly intermolecular pores (Liu et al., 2013; Zhou et al., 2015). Therefore, high-rank coal has more complex and changing pore structure with smaller pore size and lower permeability. As a result, the exploration and exploitation of CBM in high-rank coal is more difficult. The better understanding of the structure and desorption-diffusion-seepage networks of high-rank coal reservoirs is one of the key factors that play a critical role in geologic evaluation and development of effective CBM technology for high-rank coal reservoirs. This has been a bottleneck issue, particularly in China, because China has a mass of high-rank coal and current CBM in China is mainly produced in high-rank coal reservoirs.

There are generally four categories of pores in high-rank coal, i.e. primary pores (e.g. plant tissue pores and intergranular pores), epigenetic pores (e.g. breccia pores, fragmented pores, and friction pores), coalification-related pores (e.g., gas pores and intermolecular pores), and mineral-related pores (e.g. dissolution-created pores, intercrystalline pores, and moldic pores) (Chen et al., 2015; Mastalerz et al., 2008; Liu et al., 2015b; Yu et al., 2012; Zhang, 2001). These pores can be mainly investigated by traditional methods such as the mercury intrusion method, nitrogen adsorption, and electron microscopy. However, as widely known, the mercury intrusion method and nitrogen adsorption are focused on quantitative research of pore diameter distribution; and the electron microscopy can be used for two-dimensional (2D) morphology observation and analysis of genetic types of pores in coal. Thus, traditional methods do little to connectivity analyses of pores in coal. Recently, new techniques such as Focused Ion Beam-Scanning Electron Microscopy (FIB-SEM) and X-ray Computed Tomography (X-ray CT) have been successfully applied to study the pores in conventional reservoir and gas shale (Clarkson et al., 2013; Radliński et al., 2009; Wang et al., 2013; Yao et al., 2011). While X-ray CT has been applied to study the pores in coal seams (Ramandi et al., 2016; Pant et al., 2015; Golab et al., 2013; Yao et al., 2009;), FIB-SEM has not been widely used in coal seams. Such techniques can provide nondestructive measurements, and more importantly, the digital characterization to generate three-dimensional (3D) pore structure of coal in the scale of macropore and mesopores. It is believed that primary pores are hard to find in high-rank coal (Zhang, 2001). Epigenetic pores are considered to be disconnected pores and usually exist in form of the isolated holes on the surface of

coal observed under electron microscopy (Liu et al., 2015b; Zhang, 2001). The most important seepage pores in high-rank coal are coalification-related pores and mineral-related pores, especially gas pores, dissolution-created pores, and intercrystalline pores (Liu et al., 2015b; Zhang, 2001). Some researchers believe that coalification-related pores are the most important interconnected pores in high-rank coal (Liu et al., 2015b; Sang et al., 2009). These pores form the main channels for gas migration. Intercrystalline pores are micropores between mineral grains (Zhang, 2001). These pores have great significance for gas adsorption (Clarkson and Bustin, 1999; Permana et al., 2013; Pillalamarry et al., 2011). Other researchers think that pores are connected by microscopic fractures with different sizes (Clarkson et al., 2013; Liu et al., 2015b; Zhang et al., 2010). In addition, there are two main genetic types of high-rank coal: hypozonal metamorphism and regional metamorphism (Moore, 2012; Sang et al., 2009). Research shows that high-rank coal formed from hypozonal metamorphism has poor connectivity because of the lack of mesopores and macropores (Moore, 2012; Sang et al., 2009). Their mesopores and macropores are usually closed and damaged because of the stress caused by high burial depth. Connectivity and pore structure of high-rank coal formed from regional metamorphism have not been studied specifically. But this coal has a different coal-forming environment with high-rank coal formed from hypozonal metamorphism. Their connectivity and pore structure may also have significant differences. Therefore, the types of pores that mostly contribute to connectivity in coal, particularly in high-rank coal, are not clear, including the appearance of interconnected pores and their connectivity. Due to the poor understanding of interconnected pores of coal, it is challenging to correctly implement migration model, flow pattern, and output form of coalbed methane in coal. This limits our understanding of CBM exploitation and hinders the development of CBM exploration.

In this paper, an integrated approach combining traditional characterizing methods for macropore and mesopore with new nondestructive techniques using X-ray CT scanner and FIB-SEM was employed to accurately describe the interconnected pores and pore connectivity in high-rank coal. The coal samples used are collected from the southern Qinshui basin - a typical high-rank coal reservoir formed from regional metamorphism and a major region for the commercial development of CBM in China. The growth characteristics and genetic types of pores in the high-rank coal are also discussed. The study aims to provide a better understanding of the characteristics of interconnected pores in coal, which can guide the implementation of well stimulations and the optimization of the production systems of CBM wells in the field.

2. Materials and methodology

2.1 Samples

Two coal samples used in this study were systematically collected from the southern Qinshui basin in China: anthracite from the Bofang Mine and lean coal (semi-anthracite coal) from the Yuwu Mine, defined as Coal #1 and Coal #2, respectively. These coal samples were both selected from coal seam #3 of the Shanxi formation. Coal seam #3 in the southern Qinshui basin was formed from regional metamorphism in the Yanshanian period (denoted as Yanshanian tectonic thermal motion). Both coals are typical high-rank coal formed from regional metamorphism. The collection, retention, and preparation of the coal samples were conducted in line with the relevant standard GB/T 19222-2003 in China (Zhong et al., 2003) and international standard ISO 7404-2:1985. To prevent these coal samples from further oxidation, the coal samples collected from working faces of coal mines were wrapped using absorbent paper and hermetically sealed in plastic bags at 5°C. The key properties of these coal samples are shown in Table 1.

Table 1. Properties of coal samples used.

2.2 Pore size characterization

Pore diameter distribution, 2D morphology observation and analysis of genetic types of pores in coal are investigated by traditional methods, including mercury intrusion measurement, nitrogen adsorption test, and scanning electron microscopy analysis.

(1) Mercury intrusion measurement

The mercury intrusion method was used to analyze pore sizes from 3 to 130,000 nm. The mercury injection experiment was carried out with the AutoPore IV 9500 made by Micromeritics Instrument, USA, following ISO 15901-1:2005. Samples used for the mercury injection experiment were small coal particles of 3-4 cm^3 in volume approximately. The mercury was filled at pressures from 0.0099 to 413.46 MPa. The pore diameter was calculated using the Washburn equation (Washburn, 1921), and a surface tension of 0.48 N/m and a contact angle of 130º between coal and mercury were used. The mercury porosimetry data were used to evaluate the fractal dimension of coal samples and the pore structure (Debelak and Schrodt, 1979; Friesen and Mikula, 1988; Liu et al., 2015; Hu et al., 2004; Yao et al., 2008). The principle applied to the fractal analysis of coal by means of the mercury porosimetry measurement can refer to the literature published by Debelak and Schrodt (1979), Friesen and Mikula (1988) and Liu et al. (2015a).

(2) Nitrogen adsorption test

The nitrogen adsorption method was used to analyze pore sizes from 1 to 110 nm. Micropores smaller than 1 nm in width could not be measured. The nitrogen adsorption experiment was performed on the automated surface area and pore size analyzer TriStar II 3020 made by Micromeritics Instrument, USA, according to ISO 15901-2:2006 and ISO 15901-3:2007. Coal samples with a 45- to 60-mesh particle size were used for the adsorption experiments. Nitrogen was used as the adsorbate, at an analysis bath temperature of -195.85 ºC. The surface area of each pore was calculated using the Brunauer-Emmett-Teller (BET) theory, and the pore distribution was calculated using the Barrett-Joyner-Halenda (BJH) equation (Clarkson et al., 2013; Clarkson and Bustin, 1999; Crosdale et al., 1998).

(3) Scanning electron microscopy analysis

Pores and minerals in coal were investigated using an environment scanning electron microscope (ESEM) and field emission scanning electron microscope (FESEM) with an energy dispersive spectrometer. Pores and minerals > 0.1 μm in width were measured using the ESEM Quanta 250 produced by the FEI Company, USA, with amplification from 10^3 to 10^4. Pores and minerals > 20 nm and < 5 μm in width were measured using the FESEM SUPRA 55 produced by the Carl Zeiss Foundation Group, Germany, with amplification from 10^3 to 10^5.

Samples used for scanning electron microscopy were bulk coal. Coal samples were polished into little lumps approximately 10 mm across and 2-3 mm high using a polishing and burnishing machine. Then, the little lumps of coal were polished using a cross section polisher. Coal is known as a non-conducting substance. Therefore, to achieve better experiment results, coal samples were spluttered with a thin gold coating. Pores were observed using the high vacuum mode and minerals were analyzed via surface energy spectrum analysis.

2.3 Pore network modeling

A three-dimensional (3D) model of the pore network of coal samples was established using the X-ray CT scanner Xradia 520 Versa and the FIB-SEM Crossbeam 540 produced by the Carl Zeiss Foundation Group. Samples for the X-ray CT scan and FIB-SEM were both small coal pillars of approximately 2 mm in diameter and 2 mm in height. These were drilled to form bulk coal using the mechanical sampler. Small coal pillars were drilled to on the direction orthogonal to the bedding surfaces. The network formed by interconnected pores and mineral distributions of small coal pillars were firstly digitalized by X-ray CT scan at a given resolution. This provides the detailed information for re-constructing the 3D pore network of the coal sample. Then FIB-SEM was applied to emphasize the types of pores > 10 nm in width.

X-ray diffraction (XRD) was further employed to analyze the content and sort of minerals in the coal samples. Then, the interconnected pores and pore connectivity of coal samples were accurately described combining 3D model of the pore network and minerals analysis.

(1) X-ray CT scanning

The scanning area of the X-ray CT scan was 2 mm in diameter and 1 mm in height. The total scanning numbers were 3600. The pixel resolution was 1 μm and the spatial resolution was 200 nm.

The X-ray CT scanning provides structural information for development of a 3D pore network model of the coal samples at a cubic size approximately 300 μm on each side. The process of establishing the 3D model of the pore network using the X-ray CT scanner includes serval steps such as 3D imaging reconstruction, image denoising, image binaryzation, and model construction, which are beyond of the scope of this paper and details can be referred from elsewhere (Yan et al., 2000; Vincent and Soille, 1991). The 3D model of the pore network was established using the Avizo 7 which is the professional software for 3D digital core.

(2) FIB-SEM scanning

Samples for FIB-SEM were the same as those for the X-ray CT scan. The small coal pillars were polished using the cross section polisher to grind off the oxide layer (approximately 1-2 μm thick) of the coal pillars, and were not spluttered with a gold coating and other materials. The process of establishing the 3D model of the pore network using the FIB-SEM is almost the same as X-ray CT scanner, including FIB-SEM scanning, imaging, image denoising, image binaryzation, and model construction. The 3D model of the pore network was also established using the Avizo 7.

Coal samples firstly are etched and scanned by ion beam, producing a series of SEM images of the cross sections every ion beam etching. During scanning using FIB-SEM, special attention was paid to both organic matter and minerals by looking for the minerals firstly and then searching for the pores from minerals to organic matter. Thus all two categories of pores in coal samples, i.e. coalification-related pores (e.g. secondary gas pore and shrinkage-induced pore) and mineral-related pore (e.g. dissolution-created pores and intercrystalline pores), usually investigated only by ESEM and FESEM, can be identified by FIB-SEM. To emphasize mesopores, the resolution of scanning should be better than 10 nm to include mesopores < 10 nm in width, and the scanning area of the FIB-SEM should contain macropores > 5 μm in width. As a result, the range of observation of FIB-SEM includes almost all of the macropores and mesopores of interest to this study. In addition, for comparing the 3D models of X-ray CT and FIB-SEM, the scanning area of the FIB-SEM was selected in scanning area used by the X-ray CT. The scanning area of the FIB-SEM was 7.8×7.8 μm and the total scanning thickness was 9.0 μm. The total scanning numbers were 600, which meant that the single layer scanning thickness was 15 nm. Therefore, pores and minerals > 10 nm and < 5 μm in width were scanned using the FIB-SEM, with amplification from 10^3 to 2×10^5. Then, we use the same method as X-ray CT scan to remove noise of SEM pictures, binarize, and segment SEM pictures. Finally, spatial structures and pore network models of coal samples are established using Multiple-point geostatistics. In this study, the spatial resolution (X×Y×Z) of the 3D model of the pore-fracture network of coal samples was 9.8×9.8×15 nm.

2.4 Mineral analysis with XRD

The XRD experiments were conducted using the D8 Advance X-ray diffractometer made by the Bruker Company, Germany. The coal samples used for the XRD experiments were the coal with a particle size of < 325-mesh (0.045 mm). The experimental data from XRD were analyzed using Total Pattern Solution software, which is also produced by the Bruker Company. Analysis procedure of XRD pattern is as follows.

a) XRD pattern denoising and background deduction. XRD pattern is usually not smooth because of the noise. Before the analysis, we use Quadratic function fitting to remove noise and smooth XRD pattern, and

then, adjust the position of the background line and remove the background area under the background line.

b) Peak finding. Peak finding is an important step for XRD analysis. Its goal is to identify the real peak in XRD pattern and mark the position of peak.

c) Phase qualitative analysis. Each phase has its own diffraction spectrum. After peak finding, XRD patterns of coal samples can be contrast with the Powder diffraction file (PDF) standard card. Therefore, we can search out all the phases in coal samples and import structured data of phases.

d) XRD pattern fitting. In order to obtain the semiquantitative analysis results of pahses, XRD pattern also need to be fitted. XRD pattern fitting is to express diffraction curve as a functional form. In this study, we use Gaussian curve to fit diffraction peak. The fitting error should be less 9 %.

3. Results and discussion

This study uses a pore structure classification system proposed by International Union of Pure and Applied Chemistry (IUPAC), defining the pores as micropores (< 2 nm in width), mesopores (2-50 nm in width) and macropores (> 50 nm in width) (Moore, 2012; Pierotti and Rouquerol, 1985).

3.1 Pore structure

Mercury intrusion analysis is used to study macropores and some mesopores. Nitrogen adsorption analysis focuses on some micropores, mesopores and some macropores. When using mercury intrusion data to characterize the pore structure, crushing method and grinding process significantly affect the macropore size distribution at low pressure (Diduszko et al., 2000; Liu et al., 2015a; Mahamud et al., 2003; Radliński et al., 2009). High pressure compress coal or damage some existing pore walls and cause changes in intruded mercury (Diduszko et al., 2000; Liu et al., 2015a; Mahamud et al., 2003; Radliński et al., 2009). It has been reported that the pore network of coal has fractal characteristics (Diduszko et al., 2000; Liu et al., 2015a; Mahamud et al., 2003; Radliński et al., 2009). Therefore, fractal dimension analysis is usually used to examine and measure the mercury intrusion data. Three values of fractal dimension D (D1, D2, and D3) have been found for characterization of the fractal features of coal for the particle coal samples (Friesen and Mikula, 1987; Liu et al., 2010, 2015a; Mahamud et al., 2003). Different from those observed using particle coal samples, the effect of the crushing and grinding process may be ignored when using lump or large particle sizes of coals (Liu et al., 2015a). Therefore, under such a condition, D1 is difficult to obtain.

The coal samples with relatively large particle sizes were used for the mercury injection experiments in this study, and thus the effect caused by the crushing and grinding processes was ignored. In this case, the mercury data can be expressed by the Log(dV/dP)-Log(P) correlations, as shown in Figure 1. The Log curves can be divided into two different regions that represent two phases of the mercury intrusion processes, i.e. intrapore filling and coal compressibility. The pressures corresponding to these two processes, defined as P_2 and P_3, were determined via fractal dimension analyses, respectively, as shown in Table 2. The pore diameters corresponding to P_2 and P_3 were d_2 and d_3 (Table 2). The bounds of P_2, P_3 and d_2, d_3 of two coal samples were almost the same, being approximately 8-9 MPa and 120-150 nm, respectively. This means that when the pressure exceeds 9 MPa, the coal begins to become compressed. Some studies have shown that the increase of intruded mercury is totally due to the compressibility of coal when the pressure exceeds 10 MPa (Diduszko et al., 2000; Liu et al., 2015a). The limit pressure of the coal compressibility is smaller than that reported by other researchers. This may be because of the large particle sizes of coals used for the mercury injection experiments in this study. The large particle sizes of coals contain numbers of fissures that are either in macro-scale or micro-scale. These fissures increase the compressibility of coal samples. According to values of d_2 and d_3, mercury injection data can mainly incarnate the characteristics of macropores, while the characteristics of mesopores are greatly affected by the compression of coal.

Figure 1. Plots of Log(dV/dP) versus Log(P) for fractal dimension analysis: a) Coal #1 and b) Coal #2.

Table 2. Mercury injection and nitrogen adsorption data of two tested coal samples.

Although the mercury intrusion data for mesopores are inaccurate due to the effect of pore compression in coal, it can be used for the reference data of pore structure. The mercury intrusion measurement shows the two coal samples from the southern Qinshui basin were relatively low in macropores (13.6 and 18.4 vol. %, respectively) and high in mesopores (86.4 and 81.6 vol. % respectively) (Table 2). The medium pore diameters corresponding to pore volume were approximately 7-8 nm (Table 2). The pores in the coal from coal seam #3 mostly mesopores.

The nitrogen adsorption tests showed the results similar to the mercury intrusion analysis. The two coal samples prioritized mesopores (72.4 and 75.8 vol. %, respectively) and then micropores (24.5 and 17.5 vol. %, respectively), with the volume percent of macropores being the smallest (3.1 and 6.7 vol. %, respectively) (Table 2). Figure 2 shows that the pore diameters of the two coal samples centered in 5-50 nm. The Coal #1 exhibits relatively low in micropores. The Coal #2 lacks micropores of approximately 1-2 nm in diameter and mesopores of approximately 2-5 nm in diameter. The amount of micropores close to or smaller than 1 nm in diameter in the Coal #2 tends to increase. However, these micropores could not be measured due to the limitation of the experimental method. The peaks of incremental pore volume of the two coal samples were distributed on 20 and 40 nm, indicating that the coal samples prioritized mesopores of approximately 20 and 40 nm in diameter. The volume percent of pores < 10 nm and > 50 nm had a decreasing tendency. As a result, the pores in the two coal samples show a bipolar distribution (Figure 2). Therefore the mesopores of approximately 10-50 nm in diameter in the two coals dominate, and other pores were not well developed. Moreover, the mesopores of approximately 10-50 nm in diameter in both the coal samples, which may be major pores for the connectivity of the coals, would play an important role in pore connectivity and gas migration in the coal. Therefore, the mesopores of approximately 10-50 nm will be specially investigated in this study, which will be discussed in details later.

Figure 2. Plots of incremental pore volume versus pore width for nitrogen adsorption: a) Coal #1 and b) Coal #2.

3.2 Genetic types of pores

The results from ESEM, FESEM, and FIB-SEM measurements suggest there were two categories of pores in the tested coal samples: coalification-related pores and mineral-related pores.

3.2.1 Coalification-related pores

There are two types of coalification-related pores in the tested coal samples: gas pores and shrinkage-induced pores.

(1) Gas pores

Gas pores are also known as thermogenic pores (Liu et al., 2015b). There were mainly secondary gas pores in the coal samples. Secondary gas pores, which are also considered as coalification-related pores, are spaces that originated from gas generation during coalification (Liu et al., 2015b; Zhang, 2001). Secondary gas pores that are macropores, mainly developed in the organic matter in coal. Pore widths (long axis, similarly hereinafter) of the gas pores are between 0.1 and 5.0 μm, majorly 0.5-2.0 μm (Figures 3a and 3b). Secondary gas pores are generally rounded and elliptic with smooth edges (Figure 3a). Few secondary gas pores are triangular or have irregular shapes with damaged edges (Figure 3a). Some secondary gas pores are short-linear, deformed and compressed due to the action of the overlying strata's high lithostatic pressure and tectonism (Figure 3b). The development of secondary gas pores is very uneven. Most of them merge to form large clusters, mainly developed in vitrinite (Figure 3a). There are also few isolated secondary gas pores

(Figure 3b). Pore widths of these pores are usually > 1 μm. These pores were developed in vitrinite with poor connectivity (Figure 3b). Secondary gas pores in pore clusters are directionally formed in long axis orientation of the elliptic secondary gas pores with zonal distribution caused by the maximum principal stress (Figures 3a). There are few connections between pore clusters that can be observed under electron microscopy. Single secondary gas pores in pore clusters mostly exist in isolation and have poor connection with other pores. Some squashed and damaged secondary gas pores are interconnected pores connected to surrounding pores or fissures.

Figure 3. Secondary gas pores in two coal samples.

(2) Shrinkage-induced pores

(a) Basic characteristics

Shrinkage pores are primary or penecontemporaneous gaps in rock (Herrmann and Bucksch, 2014). Shrinkage-induced pores developed in coal are likely shrinkage pores in rock. Shrinkage-induced pores can be found in the joints of primary minerals and organic matter. Those pores were developed around minerals and extend to organic matter (Figures 4a and 4b). Shrinkage-induced pores do not have a fixed shape (but usually in form of the irregularly rounded, elliptic, and linear shapes), and their sizes change quite randomly (Figures 4a and 4b). Pore widths of irregularly rounded and elliptical shrinkage-induced pores are < 1 μm, mainly 20-300 nm; thus, they are mesopores and macropores (Figures 4a and 4b). The widths of linear shrinkage-induced pores are mainly < 50 nm, and their lengths are between 100 nm and 10 μm; thus, they are mesopores (Figures 4a and 4b). They can also be considered as micro-fissures. Shrinkage-induced pores were mainly developed in the joints of quartz and organic matter or clay minerals (e.g., kaolinite, illite). Their sizes are affected by the granularity of minerals. The granularity of quartz and clay minerals in coal samples is small, i.e., mainly 300 nm - 5 μm, limiting the sizes of shrinkage-induced pores. Shrinkage-induced pores also merge to form pore clusters and connect to other pores (Figures 4a and 4b). Particularly, linear shrinkage-induced pores are mutually interconnected with each other, in form of either the irregularly rounded and elliptical pores or secondary gas pores (Figures 4a and 4b). In the area where minerals were developed, the shrinkage-induced pores were usually mixed with secondary gas pores (Figure 4b). Their walls are damaged and connected to a large “hole” (Figure 4a). They can also connect to the pores in minerals (Figures 4a and 4b). Therefore, shrinkage-induced pores have good connectivity and are the most important interconnected pores in coal.

Figure 4. Shrinkage-induced pores in two coal samples.

(b) Formation

Shrinkage-induced pores may have originated from gas generation during coalification, coal matrix shrinkage caused by gas desorption after the coal samples were collected, or stress relief. This means that the pores may be formed from the separation of primary minerals and organic matter due to the contraction of organic matter during the coalification, matrix shrinkage or stress relief. As reported, none directly observed the differences between microscopic characteristics of pores and matrices before and after matrix shrinkage caused by gas desorption (Levine, 1996; Ma et al., 2011; Palmer, 2009; St. George and Barakat, 2001; Yang et al., 2012). Our previous research shows that the volumetric strain, axial strain, and radial strain of high-rank coal (air-dried sample, tested at pressure of 1-4 MPa) form the southern Qinshui basin were < 125.04×10^{-4} %, 46.75×10^{-4} %, and 32.39×10^{-4} %, respectively, when the coal adsorbed CO_2 at a room temperature. With an increasing moisture content of the coal samples, the strain capacity of high-rank coal decreases. The strain capacity of high-rank coal caused by CH_4 as reported in literature (Harpalani and Chen,

1997; St. George and Barakat, 2001), is much smaller than that caused by CO_2. Figure 4 shows that widths or diameters of shrinkage-induced pores are usually > 10 nm. This suggests that matrix shrinkage is not the reason to form those pores as matrix shrinkage cannot form that many pores in that size. It is also hard to believe that shrinkage-induced pores originated from stress relief. The degree of pressure relief in the direction of the largest main stress is larger than in the direction of the smallest main stress. These can cause the same directionality of pores as that of secondary gas pores. However, as it can be seen from Figure 4, these pores have no directionality. Of course, when gas desorption or pressure relief occurs after the coal samples are collected, the matrix shrinkage and stress relief may have some influences on these pores and enlarge the open degree of pores. Therefore the shrinkage-induced pores, as defined in this study, should be one type of special gas pores originating from gas generation.

Moreover, the two opposite sides of minerals usually develops more shrinkage-induced pores than other two opposite sides, particularly linear shrinkage-induced pores (Figure 4a). This may be caused by tectonic stress. Tectonic stress at the two opposite sides of minerals is smaller than that at other two opposite sides. Shrinkage-induced pores expand along the minimum principal stress and extend along the maximum principal stress (Figure 5).

The maceral analysis (Table 3) shows that the total content of minerals of the two coal samples were, 9.6 and 7.7 vol. %, respectively. The XRD further shows that the coals prioritized clay minerals, i.e., mainly kaolinite and illite (totally 51.0 and 46.2 wt. %, respectively), followed by quartz; while the contents of carbonate minerals and other minerals were very small. The large content of quartz and clay minerals in the coals promoted the widely developed shrinkage-induced pores.

Furthermore there are two genetic types of shrinkage-induced pores. Firstly, quartz in the coals is the original mineral, formed by regional metamorphism due to the siliciclastic sediment under an abnormally high geothermal field. It is the most stable mineral, with stable chemical properties, and not affected by coal metamorphism. Quartz is hard to cement with coal. During the formation of high-rank coal, with the increase of coalification, aliphatic series, aliphatic functional groups, and side chains of aromatic condensed nuclei decline considerably (Levine, 1993). The gelified microcomponent shrinks because of dehydration and devolatilization, resulting in the separation of organic matter and quartzes. The separation of organic matter and quartzes causes the formation of shrinkage-induced pores (Figure 5). Secondly, clay minerals in coal samples are both an original mineral and secondary mineral. The secondary clay minerals mainly fill in epigenetic fractures. There are no shrinkage-induced pores around these clay minerals. The original clay minerals are synchronous with the coal formation. They are mixed in with organic matter and cemented by organic matter (Figure 4b). The original clay minerals are also formed by regional metamorphism and hydrothermal alteration or abnormal high geothermal field after deposition, weathering, and decomposition of feldspar and mica (Dai et al., 2013; Longwell, 1987). With the increase of coalification, the gelified microcomponent around and cemented to the original clay minerals shrinks; meanwhile, the gelified microcomponent separates from the original clay minerals by the difference of physical properties between the gelified microcomponent and clay minerals, finally resulting in the formation of shrinkage-induced pores (Figure 5).

Figure 5. Sketch maps of genetic models of shrinkage-induced pores: a) developed around quartz; and b) developed around clay minerals.

(σ_{max}: maximum principal stress; σ_{min}: minimum principal stress; and ξ_s: coal matrix shrinkage)

Table 3. Content of minerals measured by XRD and maceral analysis of two coal samples.

As well known, high-rank coal in the southern Qinshui basin was formed from regional metamorphism in

the Yanshanian period with a high abnormal old thermal field (Deng et al., 2007; He and Xu, 2012; Wang et al., 1994; Yang et al., 2015). Magmatic activities reached the peak during the Yanshanian orogenesis, as evidenced by voluminous plutonism and volcanism that were initiated in the Jurassic and continued into the Cretaceous (He and Xu, 2012). Large igneous activities during the Yanshanian orogenesis are deemed to be related to the regional lithospheric extension at that time (Deng et al., 2007). During the Yanshanian orogenesis, deep mantle of the Qinshui basin was very active as revealed by mantle upwelling and lithospheric thinning, which caused partial melting of lower crust and intense mantle-crust substance exchange (Deng et al., 2007). The highly abnormal geothermal field was formed under such conditions and is interpreted as the main reason for the highly mature coal formation during the Carboniferous-Permian. Hydrothermal activities of deep level were active at the top of Ordovician strata, as evidenced by extensive calcite and quartz hydrothermal veins, which elevated coal maturity close to Carboniferous-Permian ones (Deng et al., 2007).

Magmatic activities during the Yanshanian orogenesis played a major role on the formation Carboniferous-Permian coal seam in the study area. The magmatic thermal metamorphism of the Qinshui basin mainly occurred on the background of hypozonal metamorphism. During the middle-late stages of the Yanshanian orogenesis, magmatic activities formed two magmatic-metamorphic belts in Qinshui basin which are near the 35 º and 38 º north latitude (He and Xu, 2012). Two magmatic metamorphism belts are respectively located in the south and north of Qinshui basin. In the southern Qinshui basin, magmatic-metamorphic belt is located in Jincheng and Changzhi area which are also the sampling locations. Coals formed under hypozonal metamorphism are medium to low - volatile bituminous coal ($R_{o,max}$=1.2 %-1.6 %) in the sampling area. Medium to low - volatile bituminous coal turned into high-rank coal ($R_{o,max}$>1.8 %) due to the magmatic thermal metamorphism. Magmatic-hydrothermal activities during the regional metamorphism elevated the content of primary minerals and the metamorphic degree of coal around these minerals, ultimately causing the development of shrinkage-induced pores near these minerals in the research area. Therefore, the regional metamorphism of the research area is the precondition for the formation of shrinkage-induced pores.

3.2.2 Mineral-related pores

There are two types of mineral-related pores in tested coal samples: dissolution-created pores and intercrystalline pores. Widths of mineral-related pores change greatly. Different types of mineral-related pores have different pore sizes and shapes.

(1) Dissolution-created pores

Dissolution-created pores, which were developed in minerals, are spaces that originated from partial dissolution of minerals. Sizes of dissolution-created pores are usually small. There are two types of dissolution-created pores in coal samples. The first type of dissolution-created pores develops in carbonate minerals (e.g., calcite) with larger granularity and some kaolinite (Figure 6a). Widths of this type of dissolution-created pores are larger and vary between 0.2 and 1.0 μm, making them macropores. They have an irregular shape and are merged to form pore clusters. This type of dissolution-created pores usually has good connectivity with itself. However, due to the small content of carbonate minerals in coal samples, they contribute to the pore development and connectivity very limited. The second type of dissolution-created pores in coal samples was developed in quartz. Widths of this type of dissolution-created pores are smaller, usually < 50 nm, making them mesopores. Under electron microscopy, these pores are generally round and isolated with poor connectivity (Figure 4a). Part of this type of dissolution-created pores connects with shrinkage-induced pores around quartz, which may increase the coal connectivity.

Figure 6. Mineral-related pores in two coal samples.

(2) Intercrystalline pores

Intercrystalline pores usually were developed in kaolinite, illite, dolomite, chlorite, and calcite (Figures 4b and 6b). Widths of intercrystalline pores are approximately 0.2-1.0 μm or even larger. In some minerals, intercrystalline pores are well developed and have good connectivity with each other (Figure 4b). However, the numbers of them are small. Thus, they have little influence on coal connectivity. Some intercrystalline pores also connect with secondary gas pores and the shrinkage-induced pores developed in organic matter around minerals (Figure 4b). This can also increase the coal connectivity potentially.

3.3 Pore interconnection

The analyses above show that pores in the two coal samples studied are mainly at the submicron scale (0.1-1 μm) and nanometer scale (10-100 nm). Particularly, shrinkage-induced pores at the nanometer scale are most likely interconnected, which might be mainly resulted from minerals. To further confirm the influence of minerals on interconnected pores in the high-rank coal, X-ray CT scan and FIB-SEM were used to investigate the pore network in the coal with a 3D model. Due to the reason of prohibitive cost and time-consuming nature , the 3D modeling of the pore network to be discussed in this study only focuses on the coal sample #1 at the micrometer scale (1-300 μm) and nanometer (10-100 nm) to submicron (0.1-1 μm) scale (Figures 7 and 8).

Table 4. Results from X-CT and FIB-SEM for 3D modeling of the pore network using coal sample #1.

Table 4 shows the contents of organic matter, minerals, and pores in the coal sample #1 using X-ray CT scan and FIB-SEM. The high contents of organic matter and minerals in the coal created the condition for the development of all two categories of pores. However, the total content of pores in this coal sample is low. The 3D model of the pore networks (Figures 7 and 8) shows that pores merge to form pore clusters, exhibiting a good connectivity at the nanometer scale (10-100 nm). Figure 7 shows that the pores > 1 μm in width were undeveloped and not well connective. In the cubic of Figure 7, light gray denotes pores; dark blue represents minerals; and blue describes organic matter. It can be seen that the interconnected pores had a banding distribution and gathered around minerals. Organic matter far away from minerals also developed a certain amount of macropores, i.e., secondary gas pores. Figure 8 shows that the interconnected pores accumulated into thin cambered surfaces or had a banding distribution or irregular shape around a cambered surface. In Figure 8, pores, minerals, and organic matter are represented by carmine, blue, and gray, respectively; and the thickness of cambered surfaces was about 2-4 pixels, corresponding to 20-60 nm approximately. Cross sections of the cambered surfaces were mainly linear-like. Lengths of the cross sections were approximately 1-6 μm. Therefore, the cambered surfaces of the interconnected pores were the linear shrinkage-induced pores under FESEM. Figure 9 shows the shape of cambered surfaces of the interconnected pores was basically consistent with the shape of minerals, implying that the interconnected pores mostly distributed along the edges of minerals. It should point out that there were also some interconnected pores in minerals and organic matter far away from the minerals. According to the shapes, sizes, and developing sites of the interconnected pores, those pores in the coal sample were mainly mesopores developed around minerals, and should be shrinkage-induced pores. Both the mineral-related pores, consisting of mesopores and macropores, and the secondary gas pores, which are generally macropores, have a poor connectivity, although a small number of mineral-related pores and secondary gas pores might be interconnected pores by connecting with shrinkage-induced pores.

Figure 7. Reconstructed 3D model and the extracted pore network using X-CT.

Figure 8. Reconstructed 3D model and the extracted pore network with FIB-SEM.

Figure 9. The extraction process of the pore network with FIB-SEM.

Generally speaking, shrinkage-induced pores are of significance for high-rank coals formed from regional metamorphism. The well-developed shrinkage-induced pores play an important role in increasing the permeability of coal. Meanwhile, many mesopores and macropores in high-rank coal are closed or disappear because of the high degree of metamorphism. The shrinkage-induced pores become an important bridge for gas migration and output. The degree of their development and the connectivity of interconnected pores have direct bearing on CBM exploitation. Regional metamorphism in the research area promoted the development of mesopores, which are mainly shrinkage-induced pores and kept pores open. In this case, regional metamorphism greatly increases the connectivity of coal in this particular area.

4. Conclusions

Various measurements such as the mercury intrusion method, nitrogen adsorption, ESEM, FESEM, X-ray CT and FIB-SEM to investigate the macropore and mesopore in high-rank coal samples collected from the southern Qinshui basin, providing better understanding of the pore interconnection for CBM exploitation of the high-rank coal reservoir formed from regional metamorphism. While the conventional methods such as mercury intrusion and nitrogen adsorption were used for characterizing pores in high-rank coal, the nondestructive techniques including X-ray CT scan and FIB-SEM were further employed for 3D modeling of the pore network. These methods, particularly CT and FIB-SEM based 3D modeling, not only provide experimental information to investigate the details of pore structure and associated effects of minerals and organic matter in the coal, but also represents an useful tool to identify the interconnected pores in coal. The results from both the mercury intrusion and nitrogen adsorption showed that volume percent of pores in the high-rank coal of the southern Qinshui basin are dominated by the mesopores of approximately 10-50 nm in width. The volume percent of macropores is smallest in the coal. Although there might be a massive of micropores < 1 nm in width, which cannot be measured due to limitations of the currently available experimental techniques, the results from this study suggest that mesopores are the major pores for the pore connectivity in the high-rank coal formed from regional metamorphism.

Electron microscopy observations reveal there are coalification-related pores and mineral-related pores in the high-rank coals. There are two types of coalification-related pores, i.e. secondary gas pores and shrinkage-induced pores; and there are also two types of mineral-related pores, i.e. dissolution-created pores and intercrystalline pores. Secondary gas pores are macropores, mainly developed in organic matter. Although these pores merge to form pore clusters, they are usually isolated from other pores and have a poor connectivity under electron microscopy. Mineral-related pores can be both macropores and mesopores, mainly developed within minerals. They can have a good connectivity but is limited by their small content caused by small content of carbonate minerals, and hence mineral-related pores have little influence on coal connectivity. Under electron microscopy, shrinkage-induced pores are mainly mesopores, developed in organic matter and/or around quartz and clay minerals. The regional metamorphism of the high-rank coal, under a high abnormal old thermal field as known, is the precondition of the pores formation. Shrinkage-induced pores around quartz and clay minerals have different causes of formation and shapes because of the different characteristics of quartz and clay minerals. There is a large number of shrinkage-induced pores in coal samples, which exhibit a good connectivity and can be identified as the interconnected pores in the high-rank coal. This has been further confirmed in this study via 3D pore network models developed at the micrometer scale (1-300 μm) and nanometer (10-100 nm) to submicron scale (0.1-1 μm) using a representative coal sample. The investigation of the pore network further proved the quartz and

clay minerals significantly affect the development of interconnected pores in the high-rank coal.

Acknowledgments

This study was supported by the National Natural Science Foundation of China (**Nos. 41402135, 41330638, and 41272154**), the Scientific Research Foundation of Key Laboratory of Coal-based CO_2 Capture and Geological Storage, Jiangsu Province (China University of Mining and Technology) (**No. 2015A04**), National Key Basic Research Program of China (973 Program) (**No. 2009CB219608**), and Science and Technology Major Project of China National Petroleum Corporation (**No. 2013E-2205**). Engineers from the Shanxi CBM Branch of Huabei Oilfield Company and Lu'an Group and a number of research students from China University of Mining and Technology are thankful for their assistance in the coal sampling and some experiments. It is grateful to Dr. Huihu Liu from Anhui University of Science and Technology who provided useful discussion during this study.

References

Alexeev, A.D., Feldman, E.P., Vasilenko, T.A., 2007. Methane desorption from a coal-bed. Fuel 86(16), 2574-2580.

Alexeev, A.D., Vasilenko, T.A., Ulyanova, E.V., 1999. Closed porosity in fossil coals. Fuel 78(6): 635-638.

Alexeev, A.D., Vasylenko, T.A., Ul'Yanova, E.V., 2004. Phase states of methane in fossil coals. Solid State Communications 130(10), 669-673.

Bao, Y., Wei, C.T., Wang, C.Y., Li, L.C., Sun, Y.M., 2013. Geochemical characteristics and identification of thermogenic CBM generated during the low and middle coalification stages. Geochemical Journal 47(4), 451-458.

Chen, Y., Tang, D.Z., Xu, H., Tao, S., Li, S., Yang, G.H., Yu, J.J., 2015. Pore and fracture characteristics of different rank coals in the eastern margin of the Ordos Basin, China. Journal of Natural Gas Science and Engineering 26, 1264-1277.

Clarkson, C.R., Solano, N., Bustin, R.M., Bustin, A.M.M., Chalmers, G.R.L., He, L., Melnichenko, Y.B., Radliński, A.P., Blach, T.P., 2013. Pore structure characterization of North American shale gas reservoirs using USANS/SANS, gas adsorption, and mercury intrusion. Fuel 103, 606-616.

Clarkson, C.R., Bustin, R.M., 1999. The effect of pore structure and gas pressure upon the transport properties of coal: a laboratory and modeling study. 1. Isotherms and pore volume distributions. Fuel 78(11), 1333-1344.

Crosdale, P.J., Beamish, B.B., Valix, M., 1998. Coalbed methane sorption related to coal composition. International Journal of Coal Geology 35(1-4), 147-158.

Dai, S.F., Zhang, W.G., Seredin, V.V., Ward, C.R., Hower, J.C., Song, W.J., Li, X., Zhao, L.X., Kang, H., Zheng, L.C., Wang, P.P., Zhou, D., 2013. Factors controlling geochemical and mineralogical compositions of coals preserved within marine carbonate successions: A case study from the Heshan Coalfield, southern China. International Journal of Coal Geology 109-110, 77-100.

Debelak, K.A., Schrodt, J.T., 1979. Comparison of pore structure in Kentucky coals by mercury penetration and carbon dioxide adsorption. Fuel 58(10), 732–736.

Deng, J.F., Su, S.G., Niu, Y.L., Liu, C., Zhao, G.C., Zhao, X.G., Zhou, S., Wu, Z.X., 2007. A possible model for the lithospheric thinning of North China Craton: Evidence from the Yanshanian (Jura-Cretaceous) magmatism and tectonism. Lithos 96(1-2), 22-35.

Diduszko, R., Swiatkowski, A., Trznadel, B.J., 2000. On surface of micropores and fractal dimension of activated carbon determined on the basis of adsorption and SAXS investigations. Carbon 38(8), 1153-1162.

Friesen, W.I., Mikula, R.J., 1987. Fractal dimensions of coal particles. Journal of Colloid & Interface Science 120(87), 263-271.

Friesen, W.I., Mikula, R.J., 1988. Mercury porosimetry of coals: Pore volume distribution and compressibility. Fuel 67(11), 1516-1520.

Gan, H., Nandi, S.P., Walker, P.L., 1972. Nature of the porosity in American Coals. Fuel 51, 272-277.

Golab, A., Ward, C. R., Permana, A., Lennox, P., Botha, P., 2013. High-resolution three-dimensional imaging of coal using microfocus X-ray computed tomography, with special reference to modes of mineral occurrence. International Journal of Coal Geology 113, 97-108.

Gürdal, G., Yalçın, M.N., 2001. Pore volume and surface area of the Carboniferous coals from the Zonguldak basin (NW Turkey) and their variations with rank and maceral composition. International Journal of Coal Geology 48(1-2), 133-144.

Hakimi, M.H., Abdullah, W.H., Alias, F.L., Azhar, M.H., Makeen, Y.M., 2013. Organic petrographic characteristics of Tertiary (Oligocene-Miocene) coals from eastern Malaysia: Rank and evidence for petroleum generation. International Journal of Coal Geology 120, 71-81.

Harpalani, S., Chen, G., 1997. Influence of gas production induced volumetric strain on permeability of coal. Geotechnical and Geological Engineering15(4), 303-325.

He, Z.Y., Xu, X.S., 2012. Petrogenesis of the Late Yanshanian mantle-derived intrusions in southeastern China: Response to the geodynamics of paleo-Pacific plate subduction. Chemical Geology 328, 208-221.

Herrmann, H., Bucksch, H., 2014. Dictionary geotechnical engineering/Wörterbuch geotechnik (English-German/Englisch-Deutsch). Springer Berlin Heidelberg, pp 1225-1225.

Hirsch, P. B., 1954. X-ray scattering from coals. Proceedings of the Royal Society A 266(1165), 143-169.

Levine, J.R., 1996. Model study of the influence of matrix shrinkage on absolute permeability of coal bed reservoirs. Geological Society, London, Special Publications 109(1), 197-212.

Levine, J.R., 1993. Coalification: the evolution of coal as source rock and reservoir rock for oil and gas. Hydrocarbons from coal: AAPG Studies in Geology 38, 36-77.

Liu, C.J., Wang, G.X., Sang, S.X., Gilani, W., Rudolph, V., 2015a. Fractal analysis in pore structure of coal under conditions of CO_2 sequestration process. Fuel 139, 125-132.

Liu, C.J., Wang, G.X., Sang, S.X., Rudolph, V., 2010. Changes in pore structure of anthracite coal associated with CO_2 sequestration process. Fuel 89(10), 2665-72.

Liu, S.Q., Sang, S.X., Liu, H.H., Zhu, Q.P., 2015b. Growth characteristics and genetic types of pores and fractures in a high-rank coal reservoir of the southern Qinshui basin. Ore Geology Reviews 64, 140-151.

Liu, S.Q., Sang, S.X., Zhu, Q.P., Gao, H.F., Liu, H.H., Lin, L.X., 2015c. Triple medium physical model of post fracturing high-rank coal reservoir in southern Qinshui Basin. Journal of Earth Science 26(3), 407-415.

Liu, S.Q., Sang, S.X., Zhu, Q.P., Liu, H.H., Gao, H.F., 2014a. Structure and production fluid flow pattern of post-fracturing high-rank coal reservoir in Southern Qinshui Basin. Journal of Central South University 21(10), 3970-3982.

Liu, S.Q., Sang, S.S., Zhu, Q.P., Liu, H.H., 2014b. Response characteristics and mechanisms of dynamic fluid field for well interference of coal bed methane group wells in production block. Energy, Exploration & Exploitation 32(5), 771-790.

Liu, Z.H., Liu, J.G., Dong, Y.G., Chen, Y., Xing, L.R., Liu, Z.Q., 2013. Microstructure of mid and high rank coals from Qinshui Basin, North China and its contribution to coalbed meathane. Advanced Materials Research 616, 201-207.

Longwell, J.P., 1987. Mineral impurities in coal combustion: Behavior, problems and remedial measures. American Scientist 75(1), 90.

Ma, Q., Harpalani, S., Liu, S.M., 2011. A simplified permeability model for coalbed methane reservoirs based on matchstick strain and constant volume theory. International Journal of Coal Geology 85(1), 43-48.

Mahamud, M., Scar, L., Pis, J.J., Pajares, J.A., 2003. Textural characterization of coals using fractal analysis. Fuel Processing Technology 81(2), 127-142.

Mastalerz, M., Drobniak, A., Strąpoć, D., Solano Acosta, W., Rupp, J., 2008. Variations in pore characteristics in high volatile bituminous coals: Implications for coal bed gas content. International Journal of Coal Geology 76(3), 205-216.

Moore, T.A., 2012. Coalbed methane: A review. International Journal of Coal Geology 101, 36-81.

Palmer, I., 2009. Permeability changes in coal: Analytical modeling. International Journal of Coal Geology 77(1-2), 119-126.

Ramandi, H.L., Mostaghimi, P., Armstrong, R.T., Saadatfar, M., Pinczewski, W.V., 2016. Porosity and permeability characterization of coal: a micro-computed tomography study. International Journal of Coal Geology 154-155, 57-68.

Pant, L.M., Huang, H., Secanell, M., Larter, S., Mitra, S.K., 2015. Multi scale characterization of coal structure for mass transport. Fuel 159, 315-323.

Permana, A.K., Ward, C.R., Li, Z., Gurba, L.W., 2013. Distribution and origin of minerals in high-rank coals of the South Walker Creek area, Bowen Basin, Australia. International Journal of Coal Geology 116-117, 185-207.

Pierotti, R.A. and Rouquerol, J., 1985. Reporting physisorption data for gas/solid systems with special reference to the determination of surface area and porosity. Pure Appl Chem 57(4), 603-619.

Pillalamarry, M., Harpalani, S., Liu, S.M., 2011. Gas diffusion behavior of coal and its impact on production from coalbed methane reservoirs. International Journal of Coal Geology 86(4), 342-348.

Radliński, A.P., Busbridge, T.L., Gray, E.M.A., Blach, T.P., Cookson, D.J., 2009. Small angle X-ray scattering mapping and kinetics study of sub-critical CO_2 sorption by two Australian coals. International Journal of Coal Geology 77(1-2), 80-89.

Sang, S.X., Liu, H.H., Li, Y.M., Li, M.X., Li, L., 2009. Geological controls over coal-bed methane well production in southern Qinshui basin. Procedia Earth and Planetary Science 1(1), 917-922.

St. George, J.D., Barakat, M.A., 2001. The change in effective stress associated with shrinkage from gas desorption in coal. International Journal of Coal Geology 45(2-3), 105-113.

Vincent, L., Soille, P., 1991. Watersheds in digital spaces: an efficient algorithm based on immersion simulations. IEEE Transactions on Pattern Analysis and Machine Intelligence 13(6), 583-598.

Wang, B., Li, J.M., Zhang, Y., Wang, H.Y., Liu, H.L., Li, G.Z., Ma, J.Z., 2009. Geological characteristics of low rank coalbed methane, China. Petroleum Exploration and Development 36(1), 30-34.

Wang, G.L., Jiang, B., Yu, Z.W., Yan, S.X., 1994. The system of extensional structures developed in the late Yanshanian orogeny in the west of Shandong Province, China. Tectonophysics 238(1-4), 217-228.

Wang, H.P., Yang, Y.S., Wang, Y.D., Yang, J.L., Jia, J., Nie, Y.H., 2013. Data-constrained modelling of an anthracite coal physical structure with multi-spectrum synchrotron X-ray CT. Fuel 106, 219-225.

Washburn, E.W., 1921. The dynamics of capillary flow. Physical Review 17(3), 273-283.

Weishauptova, Z., Medek, J. and Kovář, L., 2004. Bond forms of methane in porous system of coal II. Fuel 83(13), 1759-1764.

Xia, W.C., Yang, J.G., Liang, C., 2013. A short review of improvement in flotation of low rank/oxidized coals by pretreatments. Powder Technology 237, 1-8.

Yan, C.H., Whalen, R.T., Beaupré, G.S., Yen, S.Y., Napel, S., 2000. Reconstruction algorithm for polychromatic CT imaging: application to beam hardening correction. IEEE Transactions on Medical Imaging 2000, 19(1), 1-11.

Yang, M.X., Fu, J.J., Ren, A.Q., 2015. Recognition of Yanshanian magmatic-hydrothermal gold and polymetallic gold mineralization in the Laowan gold metallogenic belt, Tongbai Mountains: New evidence from structural controls, geochronology and geochemistry. Ore Geology Reviews 69, 58-72.

Yang, Y., Peng, X. and Liu, X., 2012. The stress Sensitivity of Coal Bed Methane Wells and Impact on Production. Procedia Engineering, 31: 571-579.

Yao, Y.B., Liu, D.M., Cai, Y.D., Li, J.Q., 2010. Advanced characterization of pores and fractures in coals by nuclear magnetic resonance and X-ray computed tomography. Science China-Earth Sciences 53(6), 854-862.

Yao, Y.B., Liu, D.M., Che, Y.; Tang, D.Z., Tang, S.H., Huang, W.H., 2009. Non-destructive characterization of coal samples from China using microfocus X-ray computed tomography. International Journal of Coal Geology 80 (2), 113-123.

Yao, S.P., Jiao, K., Zhang, K., Hu, W.X., Ding, H., Li, M.C., Pei, W.M., 2011. An atomic force microscopy study of coal nanopore structure. Chinese Science Bulletin 56(25), 2706-2712.

Yu, Y.M., Liang, W.G., Hu, Y.Q., Meng, Q.R., 2012. Study of micro-pores development in lean coal with temperature. International Journal of Rock Mechanics and Mining Sciences 51, 91-96.

Zhang, H., 2001. Genetical type of pores in coal reservoir and its research significance. Journal of Coal Science & Engineering 26(1), 40-44.

Zhang, S.H., Tang, S.H., Tang, D.Z., Pan, Z.J., Yang, F., 2010. The characteristics of coal reservoir pores and coal facies in Liulin district, Hedong coal field of China. International Journal of Coal Geology 81(2), 117-127.

Zhong, L.W., Chen, P.Y., Ren, D.Y., 2003. China national standards: Sampling of coal petrology (GB/T 19222-2003). Standards Press of China, Beijing.

Zhou, F.B., Liu, S.Q., Pang, Y.Q., Li, J.L., Xin, H.H., 2015. Effects of coal functional groups on adsorption microheat of coal bed methane. Energy & Fuels 29(3), 1550-1557.

Highlights for Review

- Modelling three dimensional pore network model of typical high-rank coals
- Investigating growth characteristics and genetic types of pores in high-rank coals
- Shrinkage-induced pores act as the interconnected pores in high-rank coals
- The connectivity within high-rank coal is mesopore-dominated pore network

Figures

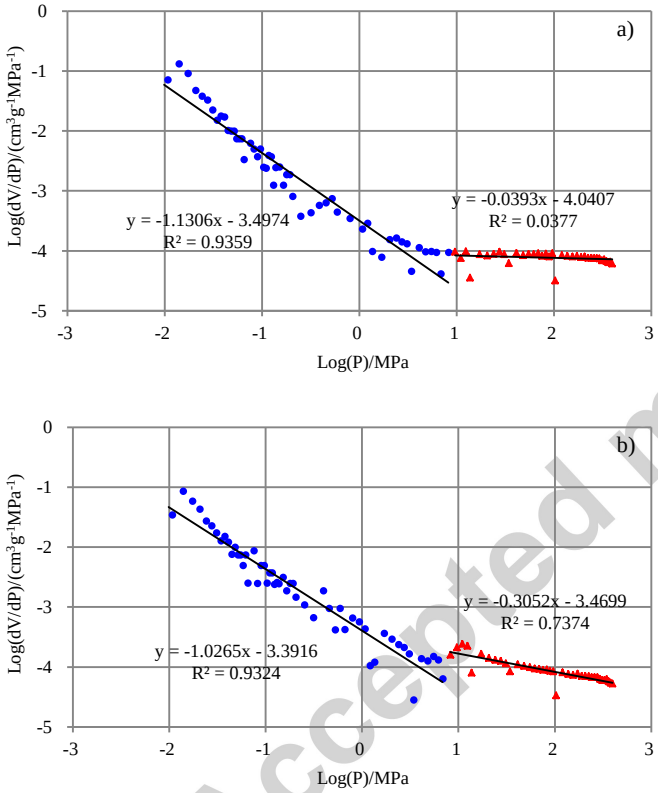

Figure 1. Plots of Log(dV/dP) versus Log(P) for fractal dimensional analysis: a) Coal #1 and b) Coal #2.

Notes: blue points are intrapore filling process; red points are coal compressibility process.

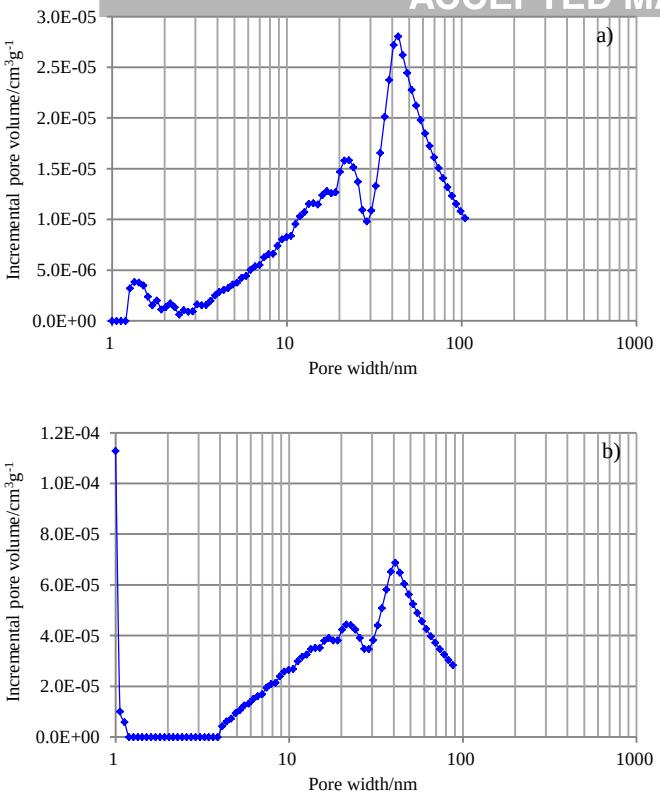

Figure 2. Plots of incremental pore volume versus pore width for nitrogen adsorption: a) Coal #1 and b) Coal #2.

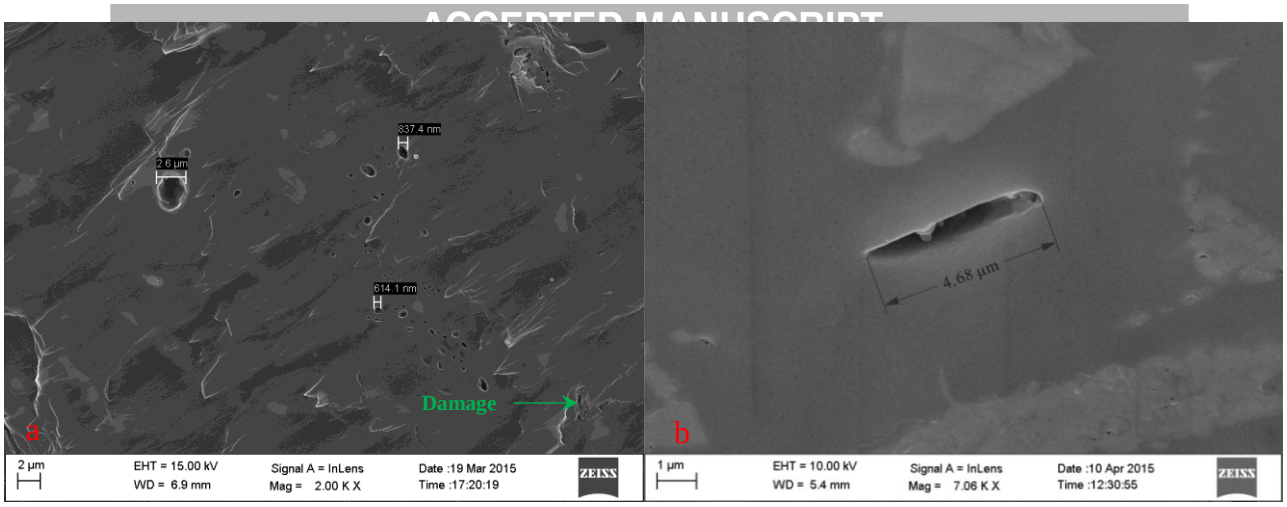

Figure 3. Secondary gas pores in two coal samples.

Notes: a, secondary gas pore groups in organic, #1 coal sample, FESEM; b, secondary gas pores with short-linear shape in organic, #2 coal sample, FESEM.

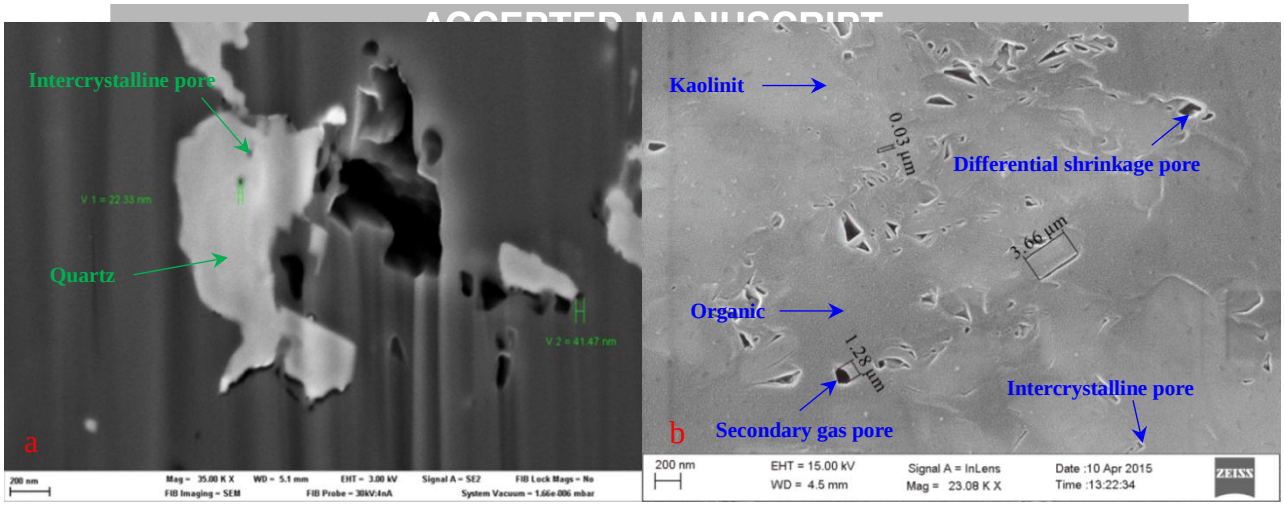

Figure 4. Shrinkage-induced pores in two coal samples.

Notes: a, shrinkage-induced pores around quartz and dissolution-created pores in quartz, #1 coal sample, FIB-SEM; b, secondary gas pores in organic, shrinkage-induced pores around clay minerals, and intercrystalline pores in clay minerals, #2 coal sample, FESEM.

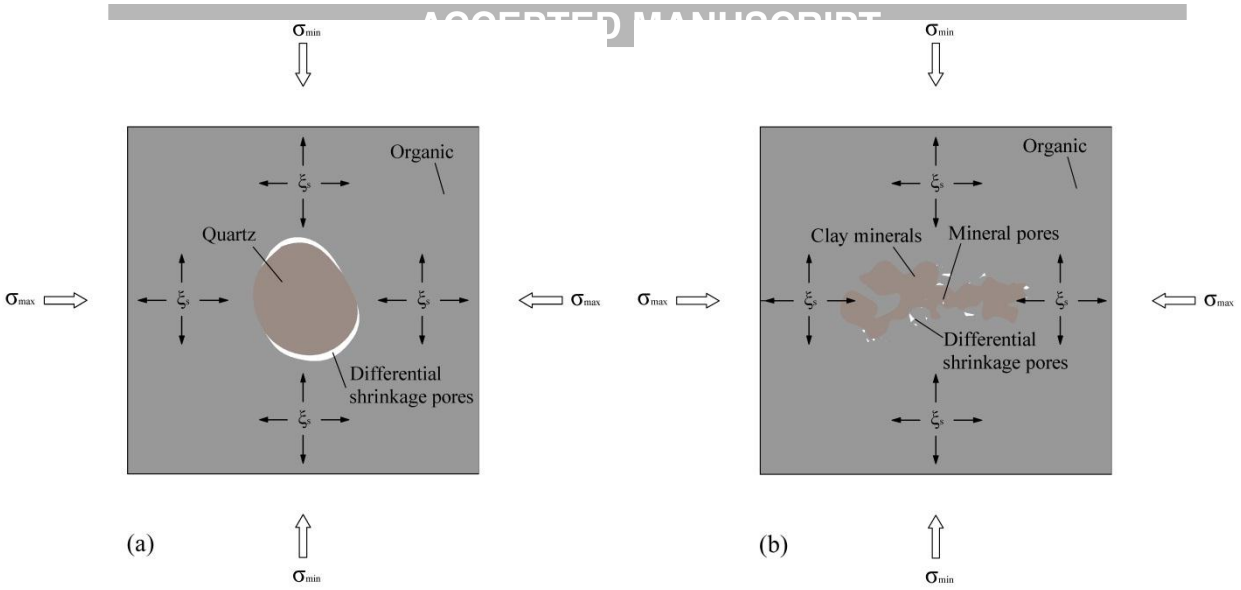

Figure 5. Sketch maps of genetic models of shrinkage-induced pores: a) developed around quartz; and b) developed around clay minerals.

Notes: σ_{max}, maximum principal stress; σ_{min}, minimum principal stress; ξ_s, coal matrix shrinkage.

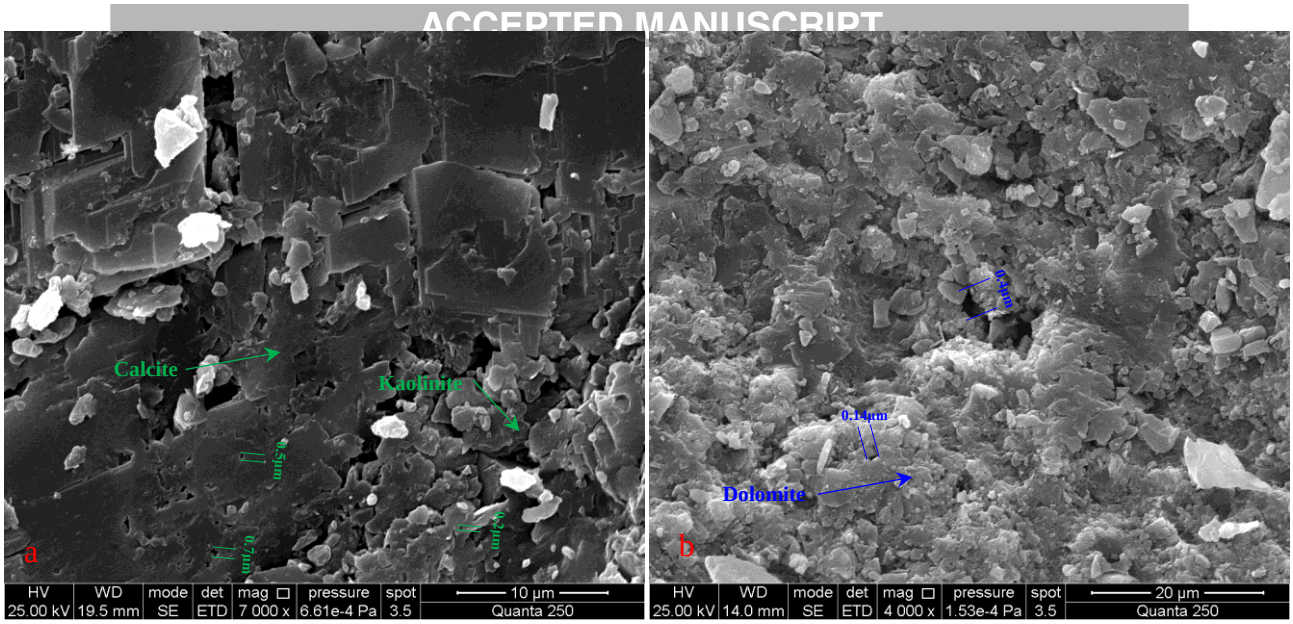

Figure 6. Mineral-related pores in two coal samples.

Notes: a, dissolution-created pores in calcite (the middle and the top left of the photograph) and kaolinite (the bottom right of the photograph), #1 coal sample, ESEM; b, and intercrystalline pores in dolomite, #2 coal sample, ESEM.

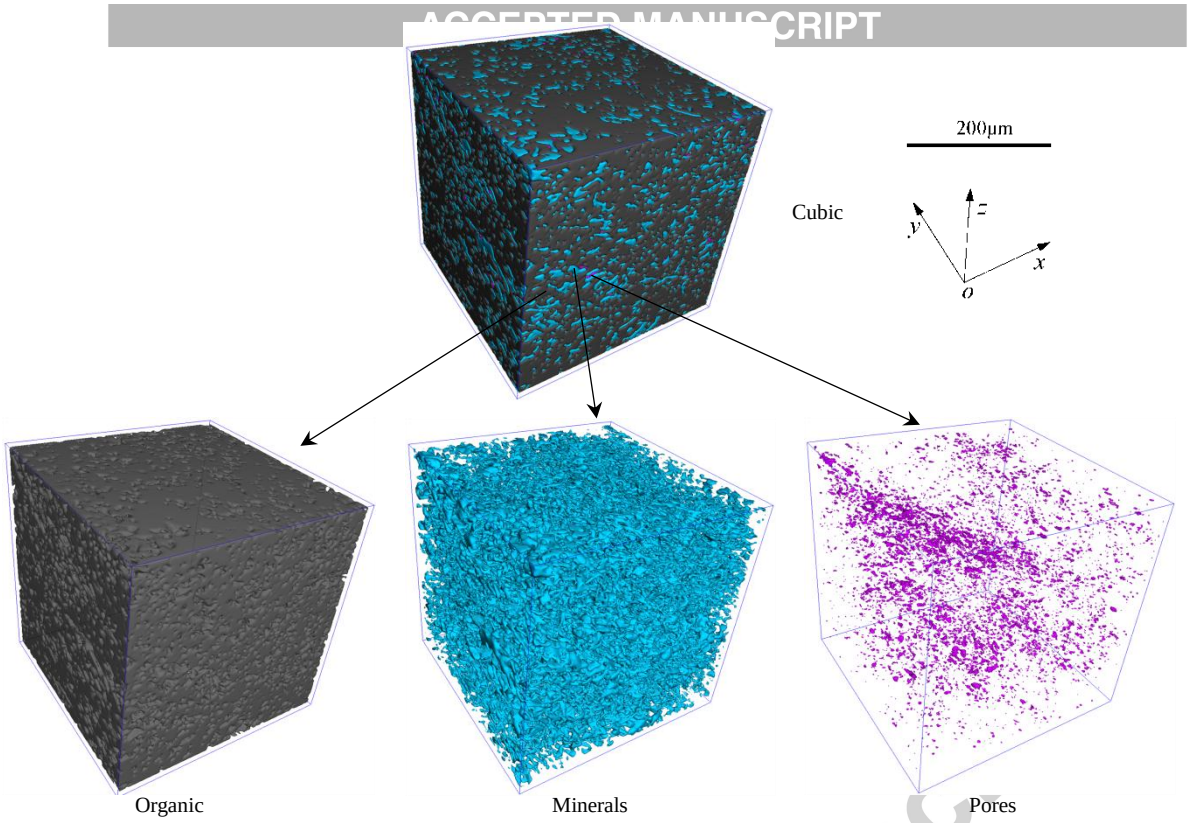

Figure 7. Reconstructed 3D model and the extracted pore network using X-CT.

Notes: In the cubic, pores are carmine; minerals are blue; and organic is gray.

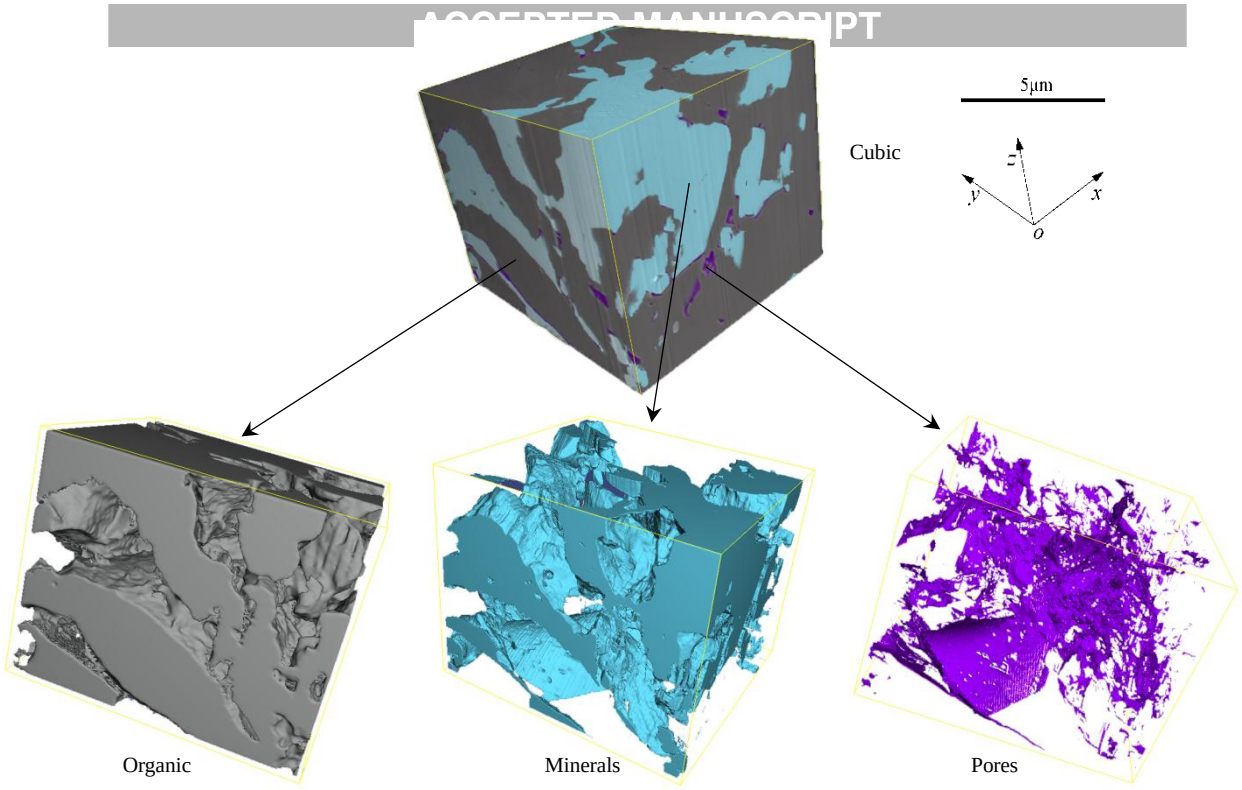

Figure 8. Reconstructed 3D model and the extracted pore network with FIB-SEM.

Notes: In the cubic, pores are carmine; minerals are blue; and organic is gray.

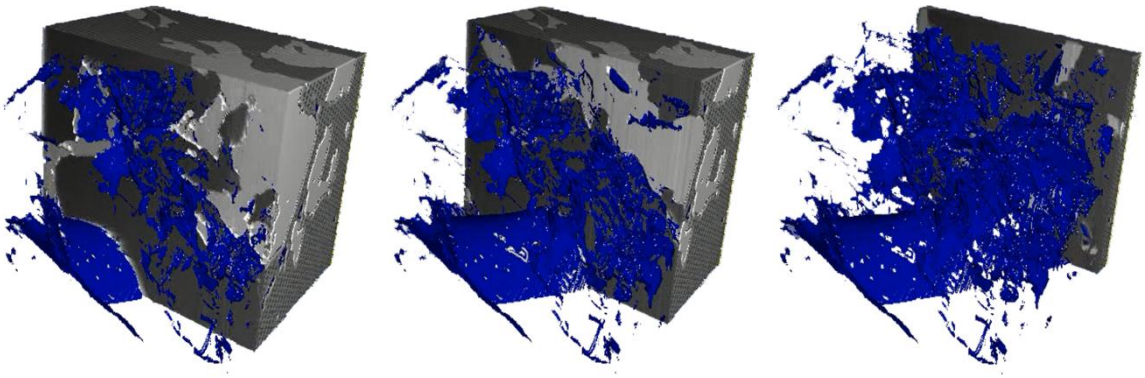

Figure 9. The extraction process of the pore network with FIB-SEM.

Tables

Table 1. Properties of coal samples used.

Samples	Sampling location	$R_{o,max}$/%	Proximate/wt. %				Ultimate/wt. %			
			M_{ad}	A_{ad}	V_{daf}	FC_{ad}	O_{daf}	C_{daf}	H_{daf}	N_{daf}
#1	Bofang Mine	2.83	2.05	9.40	9.86	81.67	2.42	91.82	3.85	1.06
#2	Yuwu Mine	2.19	1.10	11.98	13.44	76.19	2.44	91.73	4.12	1.12

Notes: wt. %, weight percent; M_{ad}, moisture, air-drying base; A_{ad}, ash yield, air-drying base; V_{daf}, volatile matter, dry ash-free basis; FC_{ad}, fixed carbon content, air-drying base; O_{daf}, content of oxygen, dry ash-free basis; C_{ad}, content of carbon, dry ash-free basis; H_{ad}, content of hydrogen, dry ash-free basis; N_{ad}, content of nitrogen, dry ash-free basis.

Table 2. Mercury injection and nitrogen adsorption data of two tested coal samples.

Samples	Fractal dimension		Pressure classification				Mercury injection data/vol. %			Nitrogen adsorption data/vol. %		
	D_2	D_3	P_2/MPa	d_2/nm	P_3/MPa	d_3/nm	V_{Me}	V_{Ma}	d_M	V'_{Mi}	V'_{Me}	V'_{Ma}
#1	2.87	3.96	<9.63	<129.6	>9.63	>129.6	86.38	13.62	7.3	24.46	72.42	3.08
#2	2.97	3.69	<8.24	<151.3	>8.24	>151.3	81.56	18.44	8.7	17.53	75.77	6.65

Notes: vol. %, volume percent; P_2, intraparticle filling; P_2, coal compression; d_2, the pore diameter corresponding to P_2; $d3$, the pore diameter corresponding to P_3; V_{Me}, volume percent of mesopores; V_{Ma}, volume percent of macropores; d_M, medium pore diameter corresponding to pore volume; V'_{Mi}, BJH pore volume percent in micropores; V'_{Me}, BJH pore volume percent in mesopores; and V'_{Ma}, BJH pore volume percent in macropores.

Table 3. Content of minerals measured by XRD and maceral analysis of two tested coal samples.

Samples	XRD/wt. %									Maceral analysis/vol. %		
	Ka	I	Ch	Fs	Do	Qz	Ru	Ba	Ap	Vitrinite	Inertinite	Mineral
#1	26.44	24.60	3.21	7.10	/	32.65	2.13	3.87	/	64.81	25.56	9.63
#2	8.21	38.00	/	2.01	1.41	33.01	3.20	/	14.16	69.74	22.56	7.70

Notes: Ka, I, Ch, Fs, Do, Qz, Ru, Ba, and Ap means Kaolinite, Illite, Chlorite, Feldspar, Dolomite, Quartz, Rutile, Bauxite, and Apatite, respectively.

Table 4. Results from X-CT and FIB-SEM for 3D modeling of the pore network using coal sample #1.

Component	X-CT		FIB-SEM	
	Volume/$\times 10^7$ μm^3	Content/vol. %	Volume/$\times 10^{11}$ nm^3	Content/vol. %
Organic	1.80	66.63	3.71	68.45
Minerals	0.68	25.24	1.63	30.07
Pores	0.22	8.14	0.08	1.48

Notes: The spatial resolution of X-CT was 200 nm, and the spatial resolution of FIB-SEM was 9.8×9.8×15 nm.